Synthetic aperture radar observation of the sea surface imprints of upstream atmospheric solitons generated by flow impeded by an island

Xiaofeng Li
NOAA, National Environmental Satellite, Data, and Information Service, Camp Springs, Maryland, USA

Changming Dong
Program in Atmospheric and Oceanic Sciences, Princeton University, Princeton, New Jersey, USA

Pablo Clemente-Colón, William G. Pichel, and Karen S. Friedman
NOAA, National Environmental Satellite, Data, and Information Service, Camp Springs, Maryland, USA

Received 16 October 2003; revised 4 December 2003; accepted 10 December 2003; published 17 February 2004.

[1] Two cases of upstream propagation of atmospheric solitons generated by atmospheric flow over topography were identified on two RADARSAT-1 synthetic aperture radar (SAR) images acquired near St. Lawrence Island in the Bering Sea on 7 September 1997 and 6 June 2001, respectively. In both cases, a group of solitons was shown as three dark-bright linear features on the SAR images. The soliton width and peak-to-peak distance measured from the two SAR images are about 3 km and 4.5 km, respectively. Simultaneous radiosonde measurements, a surface weather map and operational weather model results confirm that these waves did not propagate on the lee side of the island as is commonly observed with island lee waves, but indeed propagated against the flow in the upstream direction. In the second case, the same group of solitons was also identified as a wave-like cloud pattern on a MODIS image taken about 4.5 hours later. In this MODIS image, the soliton train propagated further upstream with the leading crest reaching about 30 km north of the island, and the number of crest-trough features increased from three to seven. In this study, we describe the generation and evolution of upstream atmospheric solitons using the Force KdV (fKdV) model with radiosonde and island topography data. The numerical solution of the fKdV exhibits a sequence of solitons propagating upstream of the island. Both temporal and spatial scales of the solitons are in good agreement with that estimated from the successive SAR and MODIS satellite images. *INDEX TERMS:* 3307 Meteorology and Atmospheric Dynamics: Boundary layer processes; 3360 Meteorology and Atmospheric Dynamics: Remote sensing; 4504 Oceanography: Physical: Air/sea interactions (0312); *KEYWORDS:* SAR, soliton, upstream

Citation: Li, X., C. Dong, P. Clemente-Colón, W. G. Pichel, and K. S. Friedman (2004), Synthetic aperture radar observation of the sea surface imprints of upstream atmospheric solitons generated by flow impeded by an island, *J. Geophys. Res.*, *109*, C02016, doi:10.1029/2003JC002168.

1. Introduction

[2] Atmospheric gravity waves can usually be generated by airflow over an island. These waves, once generated, can propagate either downstream or upstream, depending upon the atmospheric Froude number (F), stratification in the marine atmospheric boundary layer (MABL), and topographic forcing [*Baines*, 1995]. When the general characteristics of these waves can be described by the classic Korteweg-de Vries (KdV), extended KdV (eKdV) or forced extended KdV (feKdV) equations [i.e., *Miles*, 1979; *Melville and Helfrich*, 1987], they are also referred to as solitons. These waves play an important role in modifying the vertical structure of the wind, moisture, and temperature near the island, sometimes causing safety concerns and affecting aviation operations [*Christie*, 1983]. At top of the MABL, the wind field associated with the waves causes the cloud structure to change around the obstacle, allowing them to be observed in satellite visible and infrared images under conditions of high humidity such as sometimes found in maritime areas [*Gjevik and Marthinsen*, 1978; *Mitchell et al.*, 1990; *Li et al.*, 2001; *Zheng et al.*, 2004]. At the bottom of the atmospheric boundary layer, the wind velocity fluctuation at the sea surface, associated with atmospheric solitons modulates the sea surface roughness allowing imaging of these features by synthetic aperture radar (SAR) through the resonant Bragg scattering mechanism

0148-0227/04/2003JC002168$09.00

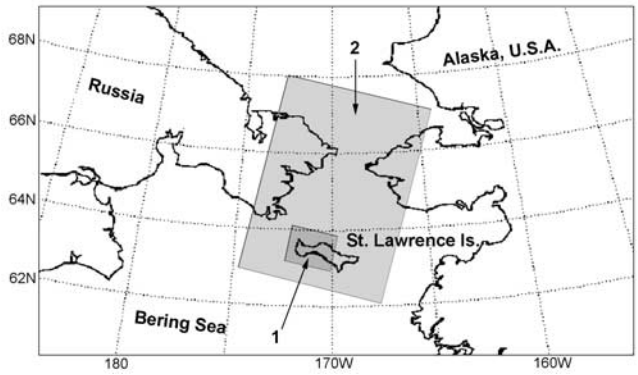

Figure 1a. A geographic map showing the study area. The SAR (Figures 2a and 2b) and MODIS image (Figure 4) coverage are indicated in the box 1 and 2, respectively. St. Lawrence Island is in the Bering Sea and in the middle of the map.

[*Valenzuela*, 1978]. Examples of SAR observations of MABL phenomena include atmospheric lee waves [*Vachon et al.*, 1994; *Li et al.*, 1998; *Zheng et al.*, 1998], atmospheric disturbances [*Alpers and Stilke*, 1996; *Mourad*, 1996], gravity waves [*Thomson et al.*, 1992; *Chunchuzov et al.*, 2000]; atmospheric boundary layer rolls and atmospheric fronts [*Johannessen et al.*, 1991; *Alpers and Brümmer*, 1994; *Mourad*, 1999; *Levy*, 2001], mesoscale phenomena such as polar mesoscale cyclones, storms, and hurricanes [*Atlas*, 1994; *Friedman and Li*, 2000; *Sikora et al.*, 2000; *Li et al.*, 2002; *Du and Vachon*, 2003], island wakes [*Pan and Smith*, 1999], cold air outbreak [*Thompson et al.*, 1983; *Mourad and Walter*, 1996], and atmospheric vortex streets [*Li et al.*, 2000].

[3] Most of the island generated atmospheric waves are lee waves, i.e., waves propagated on the downstream side of the island. Although island lee waves have been observed on SAR images from both European Remote Sensing Satellites (ERS-1/2) [*Vachon et al.*, 1994] and the Canadian RADARSAT-1 [*Li et al.*, 1998; *Chunchuzov et al.*, 2000], to our knowledge, the observation of upstream propagating solitons by SAR has been unique.

[4] The solitons that were generated and evolved upstream of the forcing occurred at the right range of Froude number, F, and forcing strength, characterized by the topography shape and height of the obstacle. *Baines* [1977] found that topographically generated upstream solitons were very strong when the flow is near resonant conditions and the amplitudes were on the order of the obstacle height. The resonant condition is defined as $F = 1$, meaning the mean flow velocity is equal to the gravity wave velocity. Later, the governing equations for describing the upstream solitons' evolution in the near resonant flow were derived as fKdV equations. *Akylas* [1984] described that upstream waves in water can be generated by moving pressure perturbation over the bottom topography. Similar fKdV equations were derived by *Patoine and Warn* [1982] for resonant forcing of Rossby waves by topography and by *Grimshaw and Smyth* [1986] for two-dimensional flow over a localized bump. For a two-layer system with rigid lid approximation, *Melville and Helfrich* [1987] derived the feKdV equation and simulated the upstream advanced solitons. With proper variable substitution, the feKdV equation can be simplified to the fKdV equation [*Baines*, 1995]. In all the cases above, the upstream soliton are above mean fluid level, meaning they are in the "elevation form."

[5] In this study, we analyze one of the first few upstream solitons observed with RADARSAT-1 SAR imagery. We simulate the upstream solitons' propagation using the two-layer fKdV equation [*Melville and Helfrich*, 1987]. SAR observations of two cases of solitons near St. Lawrence Island in the Bering Sea are given in section 2. In the second SAR observation case, a MODIS image taken approximately 4.5 hours after the SAR image is presented to show the evolution of the upstream solitons. Conventional measurements are also presented in this section. The implementation of the two-layer fKdV model is presented in section 3 with model description, numerical results, and their comparisons with the measurements made from satellite images. Discussions and conclusions are given in section 4.

2. Observations

2.1. SAR Images and Interpretation

[6] A map of the Bering Sea and SAR coverage is shown in Figure 1a. There are four major mountains on St. Lawrence Island. Among these, the highest is Mt. Kookooligit (673 m) in the middle of the island. In Figure 1b, the topographic cross section between points A and B of Mt. Kookooligit is shown.

[7] The two full resolution RADARSAT-1 SAR images (Figures 2a and 2b) considered in this study are sections of two ScanSAR Wide B scenes processed at the Alaska Satellite Facility (ASF). These images were obtained during the Alaska SAR Demonstration (AKDEMO) project, sponsored by the National Oceanic and Atmospheric Administration (NOAA). The AKDEMO is a multiyear demonstration of the production and the use of SAR quantitative and qualitative products in a pre-operational environment [*Pichel and Clemente-Colón*, 2000]. The ScanSAR wide B mode SAR image has a spatial resolution of 100 m with a pixel spacing of 50 m. RADARSAT-1 SAR is

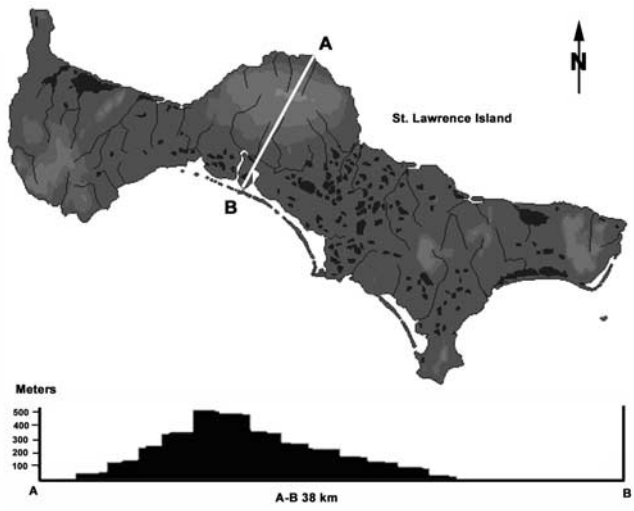

Figure 1b. A topographic cross section along the A–B line of Mt. Kookooligit on St. Lawrence Island.

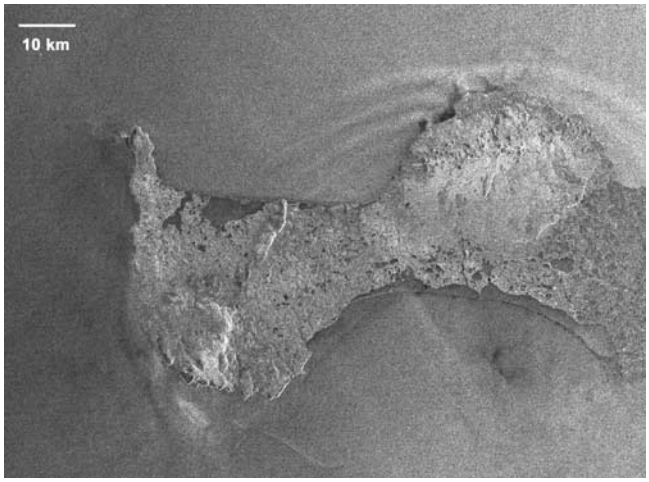

Figure 2a. A RADARSAT ScanSAR wide B mode SAR image containing the sea surface imprint of a group of atmospheric solitary waves. The image center is located at roughly N63.5° and W 172°. The image was acquired at 18:08:46 UTC on 7 September 1997 (from Canadian Space Agency, 1997, available at http://www.space.gc.ca).

a C band radar with horizontal polarization (HH). The swath width for the ScanSAR wide mode is about 500 km. In both SAR images, St. Lawrence Island is in the middle of the image, and there are three alternate bright-dark lines over the ocean surface to the north of Mt. Kookooligit, and propagating to the north toward the Bering Strait. The dark pattern in the middle of the crests represents the low backscatter from a smoother sea surface associated with lower wind speed, and the bright lines correspond to a high sea surface wind field. We interpret these features as a sea surface wind modulation pattern associated with the atmospheric solitons. The soliton width, and peak to peak distance of the solitons measured from the two SAR images are about 3 km and 4.5 km, respectively.

2.2. SAR Wind Image Retrieval

[8] The atmospheric solitons modify the low level atmospheric wind field. This wind modulation can be seen on wind images retrieved from calibrated RADARSAT-1 SAR data. This wind retrieval from SAR is dependent upon knowledge of the normalized radar cross section (NRCS) obtained from the calibrated SAR image [*Monaldo et al.*, 2001; *Wackerman et al.*, 2002]. SAR measures the variation in NRCS from the wind-roughened sea surface, which is a function of wind velocity and direction. SAR imagery has only one azimuth viewing angle; therefore, to derive the wind velocity, one must obtain the wind direction independently from another source, i.e., either from operational weather model output [*Monaldo et al.*, 2001] or from finding the wind-aligned patterns in the SAR data itself [*Wackerman et al.*, 2002]. In this study, the wind image (Figure 3) that is based on the SAR image taken on 6 June 2001 was derived using a procedure developed by the Johns Hopkins University Applied Physics Lab (JHU/APL) [*Monaldo et al.*, 2001]. This model is a based on the well-validated CMOD4 wind retrieval model [*Stoffelan and Anderson*, 1993, 1997] as

$$\sigma_0^V = a(\theta)U^{r(\theta)}[1 + b(\theta)\cos\phi + c(\theta, U)\cos 2\phi]^{\beta}, \qquad (1)$$

where σ_0^V, is the NRCS in vertical polarization (VV), U is the wind speed, θ is the local incidence angle, $r(\theta)$ is the power law dependence on wind speed, and ϕ is the angle between SAR look direction and the wind direction. The detail of the CMOD4 function is slightly different in different studies. In *Stoffelan and Anderson*'s [1993, 1997] papers, $\beta = 1.6$, while in the JHU/APL wind retrieval procedure, $\beta = 1.0$ [*Monaldo et al.*, 2001]. This variation does not affect the general solutions to equation (1) because

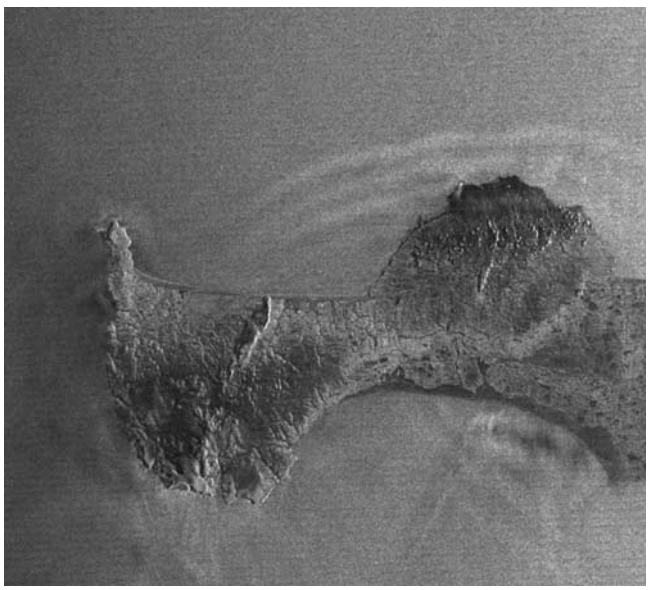

Figure 2b. Same as Figure 2a except that the image was acquired at 18:07:58 UTC on 6 June 2001 (from Canadian Space Agency, 2001, available at http://www.space.gc.ca).

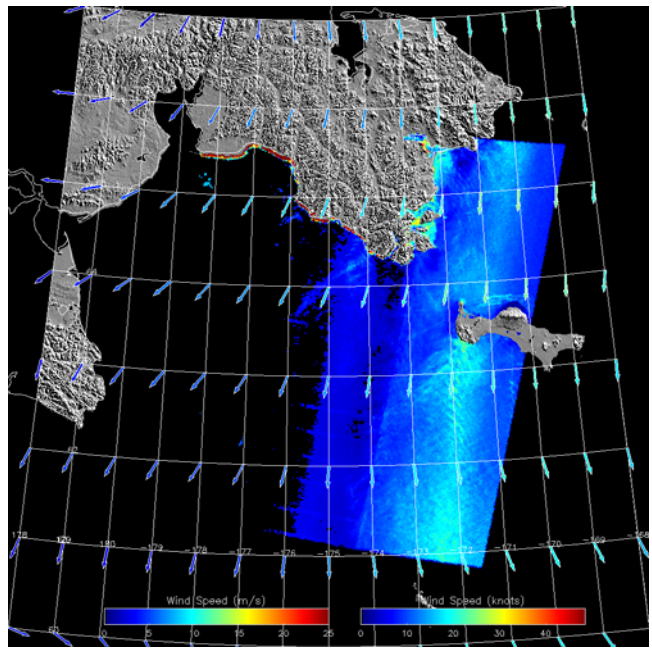

Figure 3. Wind speed image derived from SAR image.

Figure 4. The wave-like cloud pattern in the MODIS image represents atmospheric solitons. The image center is located at roughly N63.5° and W 172°. The image was acquired at 22:45:00 UTC on 6 June 2001, about 4.5 hours later than that of the SAR image in Figures 2a and 2b.

the coefficients change accordingly. The CMOD4 was developed for the ERS-1 C-band vertically polarized scatterometer (C-VV). Since the RADARSAT-1 SAR image was acquired at C-band horizontal polarization (C-HH), a wind retrieval model for C-HH was developed the JHU/APL by establishing the relationship between NRCS for C-VV and C-HH [*Thompson et al.*, 1998; *Monaldo et al.*, 2001] as

$$\sigma_0^H = \sigma_0^V \frac{(1 + \alpha \tan^2 \theta)^2}{(1 + 2\tan^2 \theta)^2}, \quad (2)$$

where α is a parameter that is still an area of research, and has been empirically estimated to be 0.6. Note for normal incidence angle, i.e., $\theta = 0$, $\sigma_0^H = \sigma_0^V$. To derive the SAR wind image in Figure 3, wind direction is obtained from the $1° \times 1°$ latitude/longitude grid NOGAPS (Naval Operational Global Atmospheric Predication System) meteorological model analysis closest in time to the SAR image. One can see from the wind image that the wind speed is about 10 ms^{-1} to the north of St. Lawrence Island and three light blue linear features (high wind) are seen radiating from the middle mountain to north. In addition, the NOGAPS wind direction, represented by arrows at grid point, is slightly to the southwest. This indicates that the solitons propagated opposite to the wind direction. The SAR imaging mechanism of the upstream solitons on the sea surface is essentially the same as that of the island lee wave case [i.e., *Vachon et al.*, 1994; *Li et al.*, 1998; *Chunchuzov et al.*, 2000].

[9] During the AKDEMO project and during the research period proceeding (from 1997 to present), we have acquired hundreds of SAR images over St. Lawrence Island, and SAR images with lee wave patterns are often found. However, the two soliton cases reported in this study are the only two upstream propagation soliton cases that we observed over the past six years. This indicates that the environmental settings (wind, atmosphere stratification, etc.) which are favorable for generating upstream propagating solitons are a rare occurrence.

2.3. MODIS Observations

[10] Figures 4 and 5 is a Moderate Resolution Imaging Spectroradiometer (MODIS) image. Its coverage is indicated in Figure 1a as Box 2. The MODIS instrument is aboard NASA's Earth Observing System (EOS AM-1) Terra satellite. This image is a MODIS band 1 (620–670 nm) solar reflectivity image with a spatial resolution of 250 m. This image was taken 4 hours 38 min later than the SAR image, and contains the same group of atmospheric solitons as in Figure 2b. Unlike the SAR image, the MODIS image can not observe anything below the cloud level; instead the MODIS image shows the cloud pattern modulation by the wind variation within the MABL. The width and peak-to-peak distance of the soliton train matches the SAR observation. At the time the MODIS image was taken, there were seven wave-like bright-dark cloud patterns on the image and the leading soliton crest reaches 30 km north of St. Lawrence Island. This indicates that the solitons propagated to the northeast. From Figure 4, one can see that there is a broad 125 km wide cloud band from the Bering Strait to St. Lawrence Island. This cloud band is as wide as the island. Such cloud patterns are generated by strong cold airflow over the warmer seawater which induces strong air sea interaction and evaporation, and resembles cold air outbreak events that happen over the Gulf Stream in the winter off the US east coast and that observed by *Mourad and Walter* [1996] in the Bering Sea. This cold airflow-passed through the Bering Strait and was mostly blocked by St. Lawrence Island. This indicates that the airflow is in the very low level of the atmosphere. The solitons were generated and propagated against the airflow in the upstream direction.

2.4. Surface Maps and Radiosonde Measurements

[11] Figures 5a and 5b show the NOAA surface analysis weather chart at the times that these two SAR images were taken. One can see that, in both cases, there were strong cyclonic systems with low pressure centered in the Gulf of Alaska. St. Lawrence Island is in the upper left corner of the

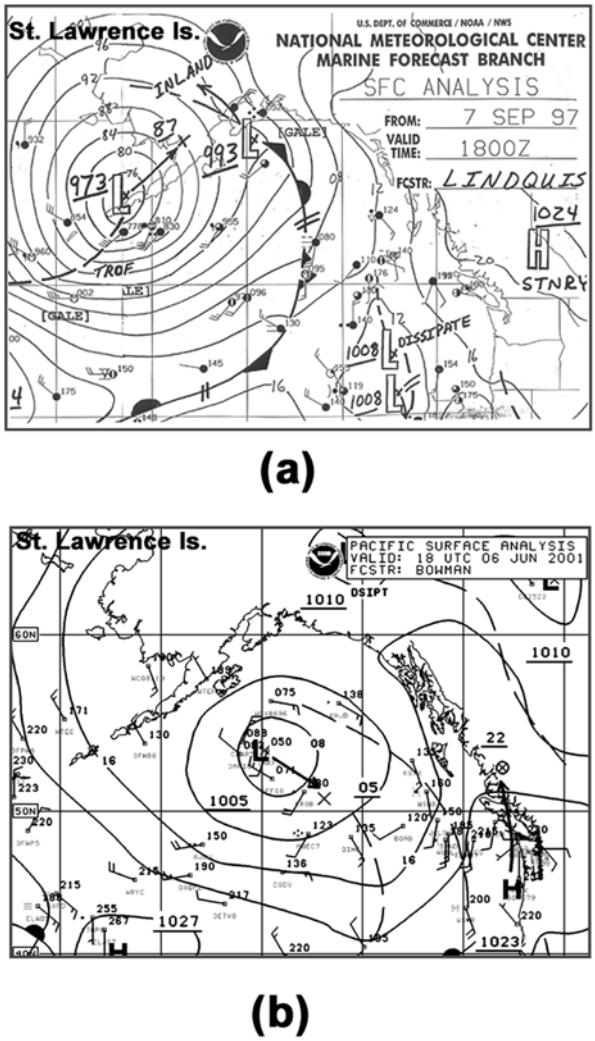

Figure 5. NOAA's surface analysis charts. Low pressure system dominated Gulf of Alaska on both maps. At the St. Lawrence Island location (upper left corner), the wind direction is to the southwest (high pressure contour line is on right-hand side), (a) NOAA surface analysis chart at 18Z on 7 September 1997; (b) NOAA surface analysis chart at 18Z on 6 June 2001.

surface weather chart, and is within the cyclonic system. The surface pressure contour lines indicate that the wind was blowing from Northeast to Southwest (with wind circulating counter-clockwise around a low pressure center in the northern hemisphere) at St. Lawrence Island which agrees with the NOGAPS model wind direction in Figure 3. As one can see from the following model analysis, the near resonant condition $F \cong 1$, can be reached when the wind speed reaches the speed of long gravity waves. A prescribed range of wind speeds is a necessary condition for the existence of this type of atmospheric solitons in the Bering Sea.

[12] The nearest upper air observation station is at Nome, Alaska, located at 64.50°N, 165.43°W. Figure 6 shows the radiosonde measurements made at 12 Z on 6 June 2001. The temperature and potential temperature profiles are represented by the solid lines. One can see that the atmospheric inversion layer height is at about the 900 mb level which corresponds to about 800 m above the ground. The near surface wind is from the NW which agrees with the surface map analyses and the NOGAPS model wind. The low level wind speed is approximately 10 ms^{-1} which agrees well with the SAR wind image (Figure 3).

[13] These observations indicate that the atmosphere was near resonant conditions when the two SAR images were acquired. The SAR image and other conventional measurements show that atmospheric solitons were not regular mountain lee waves but rather atmospheric solitons that propagated upstream against the airflow.

3. Theoretical Considerations of Upstream Soliton Dynamics

3.1. Two-Layer Forced KdV Equation (fKdV)

[14] The upstream soliton characteristics can be explained by classic Korteweg-de Vries (KdV), as well as extended KdV (eKdV) [*Miles*, 1979] or forced extended KdV (fKdV) [*Melville and Helfrich*, 1987] (hereinafter called MH) equations. The KdV equation describes one-dimensional, shallow fluid waves with small but finite amplitudes. It is also relevant to the discussion of the interaction between nonlinearity and dispersion. Theoretical considerations of this phenomenon have been described for a one layer system (fKdV) [*Akylas*, 1984; *Wu*, 1987] and a two-layer system (feKdV) by MH. By examining the radiosonde data, we can define the local atmosphere as a 2 layer system with the interface at the inversion layer height. The nondimensional two-layer forced Korteweg-de Vries equations (fKdV) is given by MH as

$$\frac{\partial \eta}{\partial t} + (F-1)\frac{\partial \eta}{\partial x} - \frac{3}{2}\delta d_{-2}\eta\frac{\partial \eta}{\partial x} - \frac{1}{6}\beta d_1 \frac{\partial^3 \eta}{\partial x^3} = \frac{\gamma F}{2\delta d_{-1}}\frac{dh}{dx}, \quad (3)$$

where η is the nondimensional interface displacement, h is the nondimensional height of the topography, $F = \frac{U}{c_0}$, the Froude number, $c_0 = \sqrt{g' h_0}$, the phase speed of linear nondispersion long wave, g' is the reduced gravity acceleration, $h_0 = \frac{d_m d_p}{d_m + d_p}$, the characteristic depth of the atmosphere, d_m and d_p are the thickness of the lower and upper layers, respectively, $\delta = \frac{a}{h_0}$, where a is the characteristic displacement of the interface, δ is the measure of nonlinearity, $\beta = \left(\frac{h_0}{l}\right)^2$, where l is the characteristic length of the topography, $\gamma = \frac{H_0}{h_0}$, where H_0 is the characteristic height of the topography, $d_n = d_-^n + (-1)^{n-1} d_+^n$, where $d_+ = \frac{d_p}{h_0}, d_- = \frac{d_m}{h_0}$.

3.2. Solution to the fKdV Equation

[15] Solutions of equation (3) are found numerically using the explicit finite difference scheme of *Vliegenthart* [1971]. In numerical experiments, we specify the values of parameters in equation (3) based on radiosonde measurements at the time the second SAR image was taken and the dimension of St. Lawrence Island. We chose this as an example because we have a MODIS image which can be used to compare results. The height of the forcing term is taken as the height of the local mountain peak, i.e., 673 m. We take the horizontal scale as 5 km. A vertical profile of potential temperature (Figure 6) shows a two-layer system

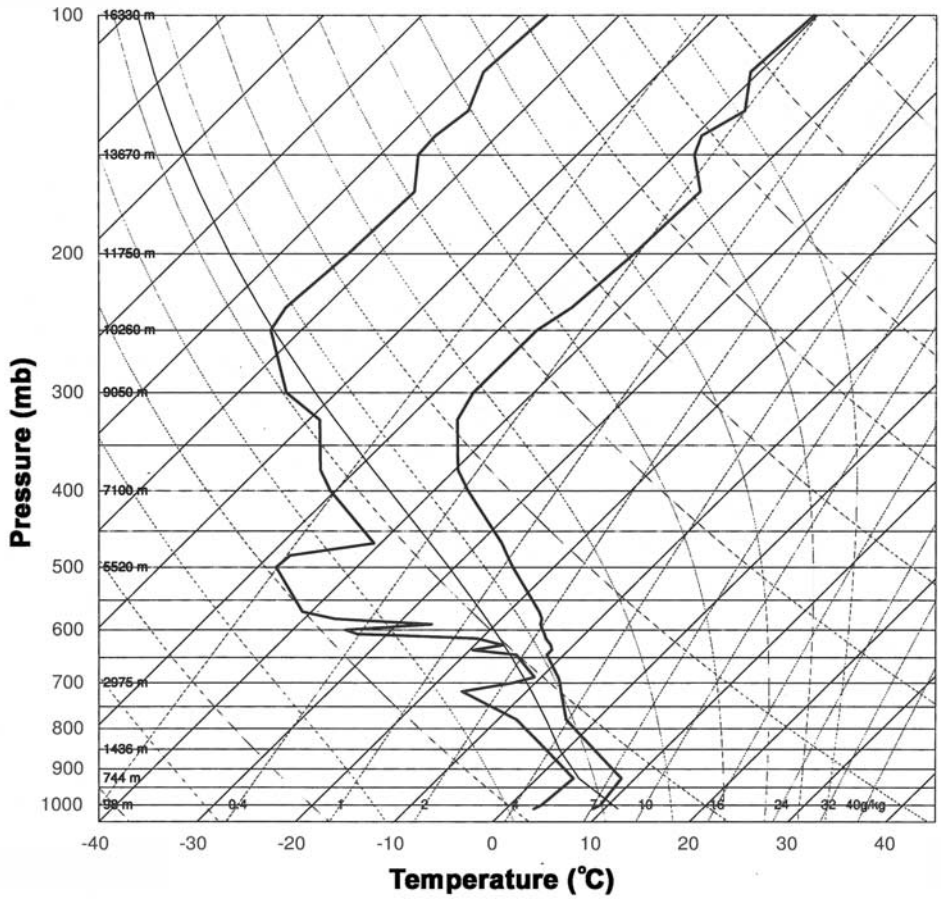

Figure 6. Radiosonde upper air observation at nearby NOME station at 12Z on 6 June 2001. The two solid lines represent the vertical profiles of potential temperature and dew point temperature.

with the interface at about 800 m. Though the radiosonde station is not on St Lawrence Island, we feel confident that we can use it to represent the atmospheric stratification as this is the closet station data available to us. Thus we set d_m = 1000 m, d_p = 4000 m. The calculated characteristic depth h_0 = 800 m, β = 0.026, and γ = 0.75 (H_0 = 673 m). The reduced gravity acceleration is g' = 0.1 ms^{-2}, so then the phase speed is c_0 = 8.9 ms^{-1}. In this study, according to the topography profile in Figure 1b, we may use the nondimensional island topography function as: $h(x) = 1 - 4x^2$ for $|x| < 0.25$, and $h(x) = 0$ elsewhere to represent the forcing term.

[16] As the basic experiment, we run the model with F = 0.95 and δ = 0.375. Figure 7 shows the nondimensional interface displacement evolves with time T. In the upstream direction ($x < 0$), at $T = 8$, two solitons appear; at $T = 24$, the fourth crest starts; by T = 40, eight crests have developed. Meanwhile, the downstream lee waves also develop and evolve with time. This wave generation pattern is consistent with the MH simulation and that of *Baines* [1995].

[17] The solitons in general have the same amplitude and are in the elevation form. Their spacing is also about the same which suggests the soliton generation rate and propagation phase velocity are nearly constant. Figure 8 displays the evolution of the upstream solitons in the dimensional time-space ($t - x$). At t = 3.0 h, the third soliton crest appears, and at t = 7.8 h, seven waves have developed. It takes

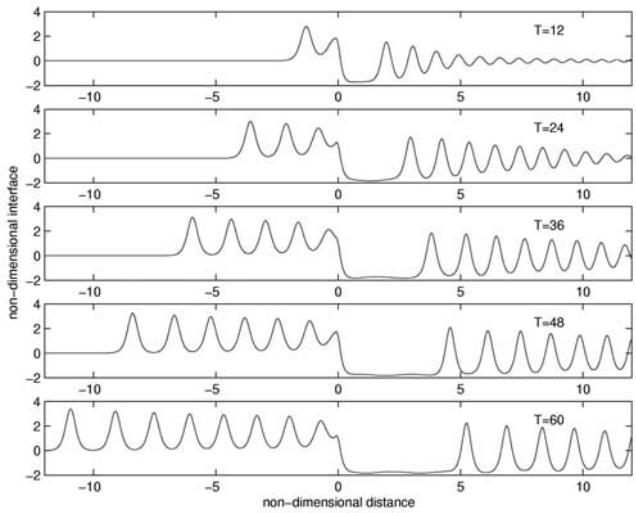

Figure 7. Basic numerical experiment: waves evolve with time for f = 0.95 and δ = 0.375. Interface displacement and horizontal distance are nondimensional. T is the nondimensional time.

4.8 hours for the soliton train to develop from 3 to 7 solitons, which is comparable to the satellite observations. The peak-to-peak distance of the soliton train is about 6.5 km and soliton width is about 2.5 km. The simulated soliton phase speed is 1.6 ms^{-1}. From the SAR images (Figure 2b) the soliton peak-to-peak distance is measured to be about 4.5 km and crest width is about 3 km. The soliton phase velocity measured by successive SAR and MODIS images is estimated to be 1.2 ms^{-1}. One can see that the simulated values agree well with the actual observation.

4. Discussion and Conclusions

[18] When strong airflows over an island or mountain, the pattern of atmospheric gravity waves depends upon the Froude number F and the characteristic height of the local topography (h). The upstream waves can occur when F is close to unity, while the lee waves can occur in a wider range of F values. This may explain why atmospheric lee waves are observed more frequently than the upstream solitons. In the neighborhood of $F = 1$, the regimes of flow over an obstacle on a $F - h$ diagram was summarized by *Baines* [1995] for hydrostatic single-layer flow and given by *Grimshaw and Smyth* [1986] for similar flow with nonlinearity and dispersion. Using the fKdV, MH has discussed in detail the dependence of the evolution of the upstream waves on the Froude number, F, and other non-dimensional parameters, and we will not repeat this discussion. Here we only show the sensitivity of the evolution of the upstream waves as a function of topography height. To examine the effect of the topography height, we run 10 experiments with H_0 varying from 100 m to 1000 m and other parameters fixed as in the basic experiment. Figure 9 shows the interface displacements at time 6.5 h for each experiment. One can see that both the wave generation rate and the wave propagation speed grow with increasing height. Wave amplitudes become weaker when the height becomes lower, and when the height is lower than a certain value, no upstream waves are generated.

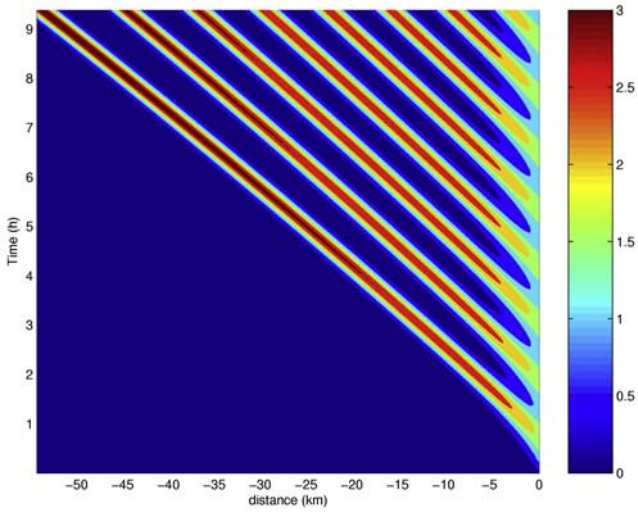

Figure 8. Wave evolvement is simulated by numerically solving the two-layer fKdV equation (3). In this figure the wave propagation is demonstrated in dimensional x-t space. The color scale represents the nondimensional interface displacement.

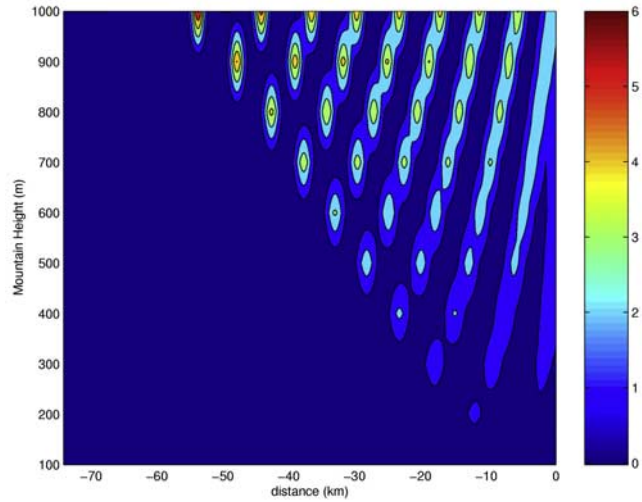

Figure 9. The sensitivity of upstream wave evolution to the topography height. −X axis is the upstream distance, and Y axis is the topography height. Non-dimensional interface displacements at the time = 6.5 hours are displayed.

[19] The modeled upstream atmospheric solitons are all in the elevation form. This is different from the commonly observed oceanic internal soliton form. The oceanic internal solitons are usually in the depression form in the open ocean where the upper layer depth is shallower than that of bottom layer. When oceanic solitons propagate into shallow water, where the upper ocean mixed layer depth equals that of the bottom layer, the soliton will switch form to become elevation solitons [*Liu et al.*, 1998]. In the atmospheric soliton case, the lower layer is usually capped by the atmospheric inversion layer and its thickness is on the order of 1 km. The upper layer is always much thicker than the lower layer. For this reason we believe no depression atmospheric solitons have been observed. In this study, no significant lee wave patterns are found. This is because the air mass from Bering Strait is very cold and dense. They flow at a very low level and most of the air was blocked by St. Lawrence Island so that the ideal conditions that we used in the model simulation do not exist in the downstream direction of the island.

[20] In summary, two cases of atmospheric upstream propagation solitons have been observed during NOAA's AKDEMO project. Compared with the frequently observed atmospheric island lee waves, these are the only two cases noted in our frequent observations over the past six years. Model data, surface maps and in situ radiosonde data all confirm that the solitons did propagate in the upstream direction and that the atmosphere was in a near resonant condition. A two-layer fKdV equation is implemented and numerically solved to simulate the generation and evolution of these solitons. The calculated soliton scale and phase velocity matched that calculated from the successive SAR and MODIS images.

[21] **Acknowledgments.** This research is funded by the NOAA/NESDIS Ocean Remote Sensing Program. The RADARSAT-1 SAR data

were obtained under the NASA RADARSAT ADRO-2 Program (Project RADARSAT-0011-0071) and processed by the Alaska Satellite Facility. The radiosonde data were downloaded from the Department of Meteorology, University of Wyoming web site at: http://weather.uwyo.edu/upperair/sounding.html.

References

Akylas, T. R. (1984), On the excitation of long nonlinear water waves by a moving pressure distribution, *J. Fluid Mech.*, *141*, 455–466.

Alpers, W., and B. Brümmer (1994), Atmospheric boundary layer rolls observed by the synthetic aperture radar aboard the ERS 1 satellite, *J. Geophys. Res.*, *99*, 12,613–12,621.

Alpers, W., and G. Stilke (1996), Observations of a nonlinear wave disturbance in the marine atmosphere by synthetic aperture radar aboard ERS-1 satellite, *J. Geophys. Res.*, *101*, 6513–6525.

Atlas, D. (1994), Original of storm footprints on the sea seen by synthetic aperture radar, *Science*, *266*, 1364–1366.

Baines, P. G. (1977), Upstream influence and Long's model in stratified flows, *J. Fluid Mech.*, *82*, 147–159.

Baines, P. G. (1995), *Topographic Effects in the Stratified Flows*, Cambridge Univ. Press, New York.

Chunchuzov, I., P. W. Vachon, and X. Li (2000), Analysis and modeling of atmospheric gravity waves observed in RADARSAT SAR images, *Remote Sens. Environ.*, *74*, 343–361.

Christie, D. R. (1983), Solitary waves as aviation hazard, *Eos Trans. AGU*, *64*, 67.

Du, Y., and P. W. Vachon (2003), Characterization of hurricane eyes in RADARSAT-1 images with wavelet analysis, *Can. J. Remote Sens.*, *29*, 491–498.

Friedman, K., and X. Li (2000), Storm patterns over the ocean with wide swath SAR, *Johns Hopkins Univ. Tech. Dig.*, *21*, 80–85.

Gjevik, B., and T. Marthinsen (1978), Three-dimensional lee-waves pattern, *Q. J. R. Meteorol. Soc.*, *104*, 947–957.

Grimshaw, R. H. J., and N. Smyth (1986), Resonant flow of a stratified fluid over topography, *J. Fluid Mech.*, *169*, 429–464.

Johannessen, J. A., R. A. Shuchman, O. M. Johannessen, K. L. Davidson, and D. R. Lyzenga (1991), Synthetic aperture imaging of upper ocean circulation features and wind fronts, *J. Geophys. Res.*, *96*, 10,411–10,422.

Levy, G. (2001), Boundary layer roll statistics from SAR, *Geophys. Res. Lett.*, *28*, 1993–1995.

Li, X., W. G. Pichel, and K. S. Friedman, and P. Clemente-Colón (1998), The sea surface imprint of island lee waves as observed by RADARSAT synthetic aperture radar, *Proc. Int. IEEE Geosci. Remote Sens. Symp.*, 763–766. Seattle, Washington.

Li, X., P. Clemente-Colón, W. G. Pichel, and P. W. Vachon (2000), Atmospheric vortex streets on a RADARSAT SAR image, *Geophys. Res. Lett.*, *27*, 1655–1658.

Li, X., Q. Zheng, W. Pichel, X. Yan, W. Liu, and P. Clemente-Colón (2001), Analysis of coastal lee waves along the coast of Texas observed on AVHRR Images, *J. Geophys. Res.*, *106*, 7017–7025.

Li, X., W. G. Pichel, M. He, S. Wu, K. S. Friedman, P. Clemente-Colón, and C. Zhao (2002), Observation of hurricane-generated ocean swell refraction at the Gulf Stream North Wall with the RADARSAT-1 synthetic aperture radar, *IEEE Trans. Geosci. Remote Sens.*, *40*, 2131–2142.

Liu, A. K., Y. S. Chang, M. K. Hsu, and N. K. Liang (1998), Evolution of nonlinear internal waves in the east and South China Seas, *J. Geophys. Res.*, *103*, 7995–8008.

Melville, W. K., and K. R. Helfrich (1987), Transcritical two-layer flow over topography, *J. Fluid Mech.*, *178*, 31–52.

Miles, J. W. (1979), On internal solitary waves, *Tulles*, *31*, 456–462.

Mitchell, R. M., R. P. Cechet, P. J. Turner, and C. C. Elsum (1990), Observation and interpretation of wave clouds over Macquarie Island, *Q. J. R. Meteorol. Soc.*, *116*, 741–752.

Monaldo, F. M., D. R. Thompson, R. C. Beal, W. G. Pichel, and P. Clemente-Colón (2001), Comparison of SAR-derived wind speed with model predictions and ocean buoy measurements, *IEEE Trans. Geosci. Remote Sens.*, *39*, 2587–2600.

Mourad, P. D. (1996), Inferring multiscale structure in atmospheric turbulence using satellite-based synthetic aperture radar imagery, *J. Geophys. Res.*, *101*, 18,433–18,449.

Mourad, P. D. (1999), Footprints of atmospheric phenomena in synthetic aperture radar images of the ocean surface: A review, in *Air-Sea Fluxes - Physics, Chemistry, and Dynamics*, edited by G. Geernaert, pp. 269–290, chap. 11, Kluwer Acad., Norwell, Mass.

Mourad, P. D., and B. A. Walter (1996), Viewing a cold air outbreak using satellite-based synthetic aperture radar and advanced very high resolution radiometer imagery, *J. Geophys. Res.*, *101*, 16,391–16,400.

Pan, F., and R. B. Smith (1999), Gap winds and wakes: SAR observations and numerical simulations, *J. Atmos. Sci.*, *56*, 905–923.

Patoine, A., and T. Warn (1982), The interaction of long, quasi-stationary baroclinic waves with topography, *J. Atmos. Sci.*, *39*, 1018–1025.

Pichel, W., and P. Clemente-Colón (2000), NOAA CoastWatch SAR Applications and Demonstration: Status and Plans, *Johns Hopkins Univ. Tech. Dig.*, *21*, 49–57.

Sikora, T. D., K. S. Friedman, W. G. Pichel, and P. Clemente-Colón (2000), Synthetic aperture radar as a tool for investigating polar mesoscale cyclones, *Wea. Forcasting*, *15*, 745–758.

Stoffelan, A., and D. Anderson (1993), Wind retrieval and ERS scatterometer radar backscatter measurements, *Adv. Space Res.*, *13*, 53–60.

Stoffelen, A., and D. Anderson (1997), Scatterometer data interpretation: Estimation and validation of the transfer function CMOD4, *J. Geophys. Res.*, *102*, 5767–5780.

Thompson, T. W., W. T. Liu, and D. E. Weissman (1983), Synthetic aperture radar observation of ocean roughness from rolls in an unstable marine boundary layer, *Geophys. Res. Lett.*, *10*, 1172–1175.

Thomson, R. E., P. W. Vachon, and G. A. Borstad (1992), Air-borne synthetic aperture radar imagery of atmospheric gravity waves, *J. Geophys. Res.*, *97*, 4249–4257.

Vachon, P. W., O. M. Johannessen, and J. A. Johannessen (1994), An ERS-1 synthetic aperture radar image of atmospheric lee waves, *J. Geophys. Res.*, *99*, 22,483–22,490.

Valenzuela, R. G. (1978), Theories for the interaction of Electromagnetic and ocean waves-A review, *Boundary Layer Meteorol.*, *13*, 61–85.

Vliegenthart, A. C. (1971), On finite-difference methods for the Korteweg-de Vries equation, *J. Eng. Math.*, *5*, 137–155.

Wackerman, C. C., P. Clemente-Colón, W. Pichel, and X. Li (2002), An analytical two-scale model to predict C-VV and C-HH radar cross section values, *Can. J. Remote Sens.*, *28*, 367–384.

Wu, T. Y. (1987), Generation of upstream advancing solitons by moving disturbances, *J. Fluid Mech.*, *184*, 75–99.

Zheng, Q., X.-H. Yan, V. Klemas, C.-R. Ho, N.-J. Kuo, and Z. Wang (1998), Coastal lee waves on ERS-1 SAR images, *J. Geophys. Res.*, *103*, 7979–7993.

Zheng, Q., et al. (2004), Evidence of upstream and downstream solitary wavetrains coexistence in the real atmosphere, *Int. J. Remote Sens.*, in press.

P. Clemente-Colón, K. S. Friedman, X. Li, and W. G. Pichel, NOAA, National Environmental Satellite, Data, and Information Service, Room 102, E/RA3 WWBG, 5200 Auth Road, Camp Springs, MD 20746, USA. (xiaofeng.li@noaa.gov)

C. Dong, Program in Atmospheric and Oceanic Sciences, Princeton University, P.O. Box CN710, 112 Sayre Hall, Princeton, NJ 08544, USA.